Applied Thermal Engineering 279 (2025) 127473

Contents lists available at ScienceDirect

Applied Thermal Engineering

journal homepage: www.elsevier.com/locate/ate

Research Paper

Experimental characterization of organic vapor flows in asymmetric curved supersonic nozzles

Marta Zocca [a,*], Paolo Gajoni [b], Alberto Guardone [a,b]

[a] Laboratory of Fluid Dynamics, School of Energy Systems, LUT University, Yliopistonkatu 34, Lappeenranta, 53850, Finland
[b] Department of Aerospace Science and Technology, Politecnico di Milano, Via La Masa 34, Milan, 20156, Italy

ARTICLE INFO

Keywords:
Nonideal Compressible Fluid Dynamics (NICFD)
Supersonic nozzles
Asymmetric nozzles
Organic vapors
Organic Rankine Cycle (ORC)
Experiments
Schlieren
Pressure measurements

ABSTRACT

An experimental campaign investigated the supersonic expansion of linear siloxane MM (hexamethyldisiloxane, $C_6H_{18}OSi_2$) in asymmetric curved planar nozzles. Two benchmark nozzle geometries were tested, both designed to discharge a parallel uniform flow of MM at Mach 1.6 under reservoir conditions characterized by a compressibility factor $Z^t = 0.40$. The nozzles feature gently-curved mean lines from inlet to outlet, discharging flow at geometric deviations of 6° and 17° from the horizontal. They differ in the shape of the channel near the minimum-area section (throat), with the first nozzle exhibiting upper and lower contours of opposite curvature, while the second nozzle has contours of concordant curvature. Shock-free expansions were observed under all tested conditions, ranging from highly nonideal ($Z^t = 0.41$) to ideal-like ($Z^t = 0.95$). Total pressure, temperature, static pressures from the inlet to the outlet, and schlieren images were recorded for each condition. A novel optical method, recently developed for asymmetric flows, enabled Mach number measurements without prior knowledge of the flow direction. The tested geometries mimic converging–diverging blade passages with a curved mean line. This study provides the first experimental validation of these asymmetric designs, previously introduced and verified only through CFD. The resulting dataset offers a valuable benchmark for validating numerical design and analysis tools in nonideal compressible flows, with direct relevance to the design of supersonic ORC turbine stages.

1. Introduction

Nonideal compressible fluid dynamics (NICFD) is a branch of gasdynamics that studies flows in thermodynamic and chemical equilibrium, specifically under nonideal conditions where the compressibility factor $Z = \frac{Pv}{RT} \neq 1$. In contrast, ideal gases satisfy $Pv = RT$, and thus $Z = 1$. Here, *nonideal* refers strictly to deviations from ideal-gas thermodynamics—not to dissipative effects such as internal friction, heat conduction, or chemical reactions. Rather, it indicates the occurrence of peculiar flow behavior because of departure from dilute, ideal-gas thermodynamics. Nonideal gasdynamic effects in single-phase flows are notable near the liquid–vapor saturation curve, at the critical point, or under supercritical conditions [1]. These flows display unique behaviors and are significant in applications like rocket propulsion [2], oil and gas applications, heat pumps, refrigeration, and pharmaceutical production [3]. In power generation, nonideal compressible fluid dynamics effects occur in supercritical carbon dioxide (sCO_2) power cycles [4] and organic Rankine cycles (ORCs) [5].

ORC power systems, suitable for power production between 10 kW and 100 MW, excel in efficiency, cost, and simplicity compared to traditional steam Rankine cycles, particularly at low (320 K to 420 K) and medium (420 K to 680 K) source temperatures. These conditions are frequently found in renewable energy sources like geothermal reservoirs, biomass combustion, and waste heat recovery from industrial processes such as power plants, cement, and glass production factories. Specifically, ORCs involve compressible flows of molecularly complex organic compounds near the liquid–vapor saturation curve and the critical point. Turbine expansion is often characterized by highly supersonic outflow and significant nonideal flow effects. Accurate design tools are essential for achieving high turbine efficiency, which significantly impacts overall cycle efficiency [6].

Experimental data on nonideal flows for Organic Rankine Cycle (ORC) applications is scarce in the open literature due to the challenges of operating specialized experimental facilities. ORC working fluids, which are typically liquid at standard room temperature and pressure, are utilized in turbine flows at saturated, superheated, or supercritical conditions, with temperatures and pressures ranging from 373 to 673 K and 1 to 5 MPa [5]. Working with organic fluids in typical operating conditions presents measurement challenges due

* Corresponding author.
E-mail address: marta.zocca@lut.fi (M. Zocca).

https://doi.org/10.1016/j.applthermaleng.2025.127473
Received 27 March 2025; Received in revised form 17 June 2025; Accepted 7 July 2025
Available online 26 July 2025

Nomenclature

μ	Mach angle [rad]
ϑ	Flow angle [rad]
^{t}	Total conditions
$_{c}$	Critical point
$_{e}$	Nozzle exhaust section
$_{t}$	Nozzle throat section
A	Area [mm^2]
d	Channel depth of planar nozzles [mm]
H	Semi-height of nozzle throat section [mm]
M	Mach number [–]
P	Pressure [Pa]
R	Gas constant [J/kgK]
R_i	Radii of circular-arc portions of nozzle contours [mm]
T	Temperature [K]
U	Measurement uncertainty, Gaussian 2σ
v	Mass-specific volume [m^3/kg]
x	Spacial coordinate along the test section axis [mm]
Z	Compressibility factor [–]

to high fluid temperatures and condensation issues, especially when replicating turbine flows near saturation. Unlike conventional cycles and turbomachinery such as gas and steam turbines, blade cascade testing for ORC applications is infrequent due to the complexities in measuring pressure levels, mass flow rates, velocity magnitudes, and their directions. Available cascade testing experiments for ORC turbine flows have included annular turbine cascade flows [7] and linear cascade flows [8]. To accurately replicate ORC operating conditions in a wind tunnel, it is necessary to employ a closed gas cycle or a phase transition thermodynamic cycle [9]. Test-rigs for ORC turbine are more complex and costly than those using incondensable gases like air, which can be managed through compressed air storage tanks or continuous loops. Furthermore, the influence of nonideal flow fields on total conditions necessitates more experimental runs for thorough characterization because process conditions significantly affect flow dynamics. In contrast, polytropic ideal gas flows in fixed geometries reveal trends in Mach number, pressure, and temperature ratios, which are fluid-dependent solely through the specific heat ratio. Over the past decade, several facilities have been commissioned to address the lack of experimental data. These include continuously operated [10–12] and intermittent [7,13–16] facilities. Refs. [1,9] provide a list of facilities used for nonideal compressible fluid dynamics experiments.

The present experimental campaign was conducted in the TROVA at Politecnico di Milano [17]. The TROVA is a blow-down wind tunnel designed to reproduce supersonic flows of organic vapors under conditions representative of ORC turbine expansions. The facility can be equipped with planar nozzles and can accommodate linear blade cascades. In this study, experiments were performed on de Laval-type nozzles, which are representative of both supersonic turbine blade passages and propulsive nozzles.

In typical supersonic ORC turbine stator channels, the desired outlet flow angle is achieved by combining a converging section with a curved mean line and a divergent section with a straight axis [18,19]. In contrast, the present study investigates planar nozzles with a continuously curved mean line from inlet to outlet. Similar geometries were explored in early air-based studies by Allen [20] and Syvertson & Savin [21], and more recently extended to nonideal flows in Ref. [22]. In Ref. [22], the authors introduced two benchmark geometries of planar asymmetric curved nozzles that differ in the shape of the channel near the throat: one type features upper and lower contours of opposite curvature (Type I), while the other has contours of concordant curvature (Type II).

As extensively emphasized in Ref. [23], a fundamental step in model validation is the assessment of its accuracy. Given that existing NICFD software tools represent some of the most powerful resources available to researchers and engineers for investigating non-ideal compressible-fluid flows and designing machinery operating in the NICFD regime, the availability of experimental data is crucial, particularly in the non-ideal thermodynamic region. This study presents the first experimental characterization of these two asymmetric benchmark geometries in the nonideal regime, which had previously only been verified through CFD. Using siloxane fluid MM (hexamethyldisiloxane, $C_6H_{18}OSi_2$), the nozzles were tested at conditions targeting an exit Mach number of 1.6, typical of ORC turbine vanes. Measurements included total temperature and pressure, static pressure distributions, and schlieren imaging. The tests covered a wide range of inlet conditions, with compressibility factors from 0.40 to 0.99, spanning from highly nonideal to nearly ideal thermodynamic states.

To enable flow field characterization in asymmetric geometries, where the flow direction is not known a priori, a recently developed schlieren-based method was employed [24]. This technique allows for direct extraction of Mach number and flow direction from optical images without relying on thermodynamic assumptions.

The campaign extensively explored off-design conditions to assess the flow behavior and the persistence of shock-free expansions under varying operating conditions. These insights are essential for evaluating nozzle performance and reliability in practical applications. Overall, the dataset contributes to the broader field of nonideal compressible fluid dynamics by offering experimental validation for geometries of direct relevance to turbomachinery design.

The paper is organized as follows. Section 2 details the design of the asymmetric curved nozzles, focusing on the geometry and the anticipated flow configuration. The experimental setup and instrumentation utilized in the experiments are outlined in Section 3. Results are presented and discussed in Section 4. Section 5 offers concluding remarks.

2. Planar asymmetric nozzles

Both asymmetric curved planar nozzles considered in the present study have a throat semi-height of $H = 8.4$ mm and a channel depth of $d = 18.7$ mm, giving a throat area of $A_t = 314.16$ mm^2. Fig. 1 shows a schematic of the nozzle geometries NMMC01 (Fig. 1(a)) and NMMC02 (Fig. 1(b)). The convergent section of both nozzles consists of a 5th-degree polynomial, matched with circular arcs of radius R_1 (lower profile) and R_2 (upper profile) at the geometrical throat. The divergent sections are designed using the Method Of Characteristics (MOC), with the code in Ref. [22]. Inputs include total pressure and temperature ($P^t = 23.05 \cdot 10^5$ Pa, $T^t = 537.15$ K), the working fluid (MM, hexamethyldisiloxane, $C_6H_{18}OSi_2$), the thermodynamic model (Span-Wagner Equation of State in the CoolProp library [25,26]), throat geometry (two radii of curvature $R_1 = 10H$ and $R_2 = 20H$, see Fig. 1), and exhaust Mach number ($M_e = 1.6$).

Immediately downstream of the geometrical throat, the lower portion of the divergent forms a circular arc with a radius R_1. The expansion to the desired M_e occurs upstream of curve CD. Downstream of curve CD, the upper profile of the nozzle continues with a straight line at an angle equal to the flow angle ϑ at point D. In contrast, the lower profile of the nozzle undergoes an isentropic turning of the flow from the flow angle at point C, ϑ_C, to the flow angle at point D, ϑ_D. At point E on the lower profile, $\vartheta_E = \vartheta_D$. Under design conditions, the flow at the exhaust section of the nozzle is uniform throughout the cross section. In nozzle NMMC01, the circular portions of the divergent profiles with radii R_1 and R_2 have curvatures of opposite sign (Type-I asymmetric nozzle). In contrast, in nozzle NMMC02 they have curvatures of the same sign (Type-II asymmetric nozzle). Full dimensional details of nozzles NMMC01 and NMMC02 are reported in

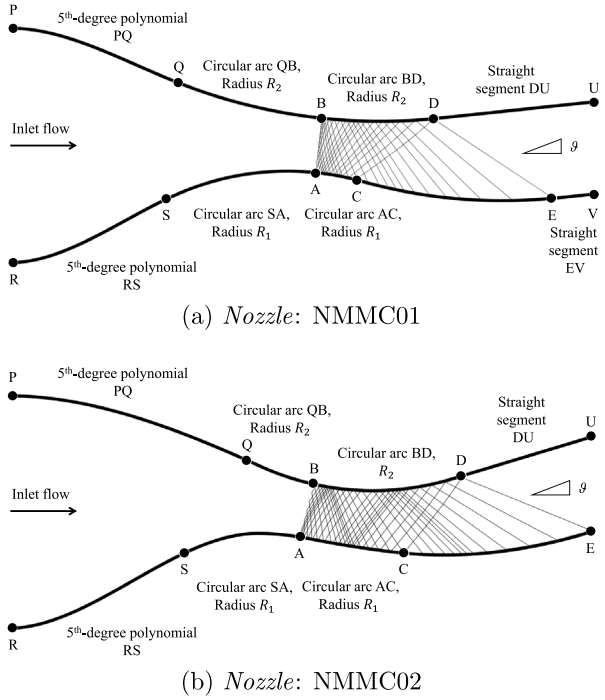

Fig. 1. Design of the tested asymmetric nozzles: (a) NMMC01, Type I, (b) NMMC02, Type II.

Fig. 4. The reader is referred to Ref. [22] for a detailed description of the divergent design procedure.

The static pressure and Mach number fields predicted by CFD simulations in both geometries are reported as contour bands in Fig. 2, confirming that a uniform parallel flow at the design exhaust Mach number is achieved at both outlet sections. Note that pressure values in Fig. 2 are reported in units of 10^5 Pa (equivalent to 1 bar), in line with customary practice in ORC-related literature and for consistency with previous experimental campaigns conducted at the TROVA facility (e.g., Ref. [17]). The same convention is followed consistently throughout the paper in all reported results. Inviscid simulations are conducted using ANSYS Fluent 21.2 over a structured computational mesh of 10k elements. The thermodynamic properties of the working fluid are modeled through Fluent interface to the RefProp library [27,28], which employs a Span-Wagner (SW) type Equation of State (EoS). The total conditions (P^t, T^t) at the inlet and a supersonic outlet are set as boundary conditions. Accuracy assessment and grid independence results for similar geometries and operating conditions are presented in Refs. [23,24]. The verification of the nozzle design code using CFD simulations is detailed in Ref. [22]. The reader is directed to these earlier works for a more comprehensive account of design routines and numerical simulation methods. While the present study focuses on inviscid flow modeling, the influence of viscous effects under the tested conditions has been addressed in previous works. As discussed in Ref. [23] and references therein, the development of a thin boundary layer along the nozzle walls has a negligible impact on the inviscid core of the flow, particularly along the horizontal axis of the test section where most measurements are taken. This observation is further supported by Ref. [24], which includes comparisons between inviscid and viscous simulations using updated tools, showing minimal differences in core flow properties for similar geometries and working fluids. These findings support the validity of the inviscid assumption adopted in the present analysis. In addition to the contour bands in Fig. 2, equally spaced black dots denote the locations where static pressures are measured in the experimental setup, as discussed in Section 3.

3. Experimental setup

The Test Rig for Organic VApors (TROVA) is a blow-down wind tunnel designed to study the flow of organic fluids under conditions relevant to Organic Rankine Cycle (ORC) applications [16]. It reproduces nonideal flows of organic vapors similar to those in ORC turbine expansions. The experiments presented in this work utilize siloxane MM (hexamethyldisiloxane, $C_6H_{18}OSi_2$), a fluid commonly used in medium to high-temperature ORCs. Siloxane MM was selected for its relatively low critical pressure, high thermal stability, and ease of supercritical operation, making it particularly suitable for highlighting nonideal compressible effects. MM replaced MDM in the TROVA facility in 2017, offering comparable nonideality with improved operational manageability. Compared to halocarbons commonly used in ORC applications, such as R245fa and R1233zd, MM exhibits significantly lower critical pressure. Fig. 3 illustrates the layout of the TROVA (top), highlighting the components relevant to the subsequent discussion. In the bottom-right corner of Fig. 3, the corresponding thermodynamic cycle for siloxane MM under exemplary operating conditions is shown. The TROVA operates with a batch Rankine cycle, where the expansion occurs through the nozzle, meaning no work is extracted. A controlled volume of working fluid is isochorically heated in a High Pressure Vessel (HPV) to the desired temperature and pressure. It is then discharged through a Main Control Valve (MCV) into a Low Pressure Vessel (LPV) via a converging–diverging nozzle (supersonic test section). The vapor is subsequently condensed in the LPV and pumped back to the HPV to initiate a new test. To minimize the presence of incondensable gases in the system, each section of the test rig is brought to the saturation pressure of MM at room temperature (~5 kPa) before each critical phase of the experiment, namely before heating the HPV and the pipelines upstream of the test section, as well as before the actual blowdown.

Each test commences when the MCV opens, lasting approximately 100 s, excluding a 2-s valve opening transient. As the HPV empties, pressure and temperature decrease, covering a range of thermodynamic states from nonideal to ideal gas conditions within a single experiment. Tests end when the nozzle reaches over-expanded conditions with shock waves in the divergent section. Under these testing conditions, both the assumptions of thermodynamic equilibrium and steady flow are considered valid. The discussion presented in Ref. [29] supports the assumption of thermodynamic equilibrium, which is justified by the very short vibrational relaxation times of the working fluid molecules due to high collision frequencies, further enhanced by the large fluid density. As a result, the thermodynamic state at each sampled moment, defined by simultaneous measurements of two independent properties, can be used to compute derived thermodynamic variables using a suitable equation of state. The assumption of steady flow is supported by the fact that, during the approximately 1.5 ms flow time, the variation in total pressure and temperature due to the emptying of the HPV is minimal, on the order of 0.15% and 0.01%, respectively. These variations fall well within the measurement uncertainty of the sensors, which is approximately 0.65% for total pressure and 0.5% for total temperature. Given the 1 kHz sampling frequency, the sensors are capable of resolving changes at the millisecond scale, and no significant unsteadiness is detected within the resolution limits of the instrumentation. In other words, any faster fluctuations, if present, would be beyond the detection capability of the calibrated sensors used in this study. Furthermore, the characteristic timescales for thermodynamic relaxation are orders of magnitude shorter than the flow passage time, reinforcing the validity of the equilibrium assumption.

The test section of TROVA features nozzle profiles (top and bottom) mounted on a mirror-polished steel back plate, along with a quartz window on the opposite side for optical access (Fig. 3, bottom-left). This planar test section has a rectangular cross-section and is equipped with static pressure taps of 0.3 mm diameter machined onto the back plate. The static pressure is measured using flush-mounted piezo-resistive pressure transducers at these wall taps. Total pressure is measured in

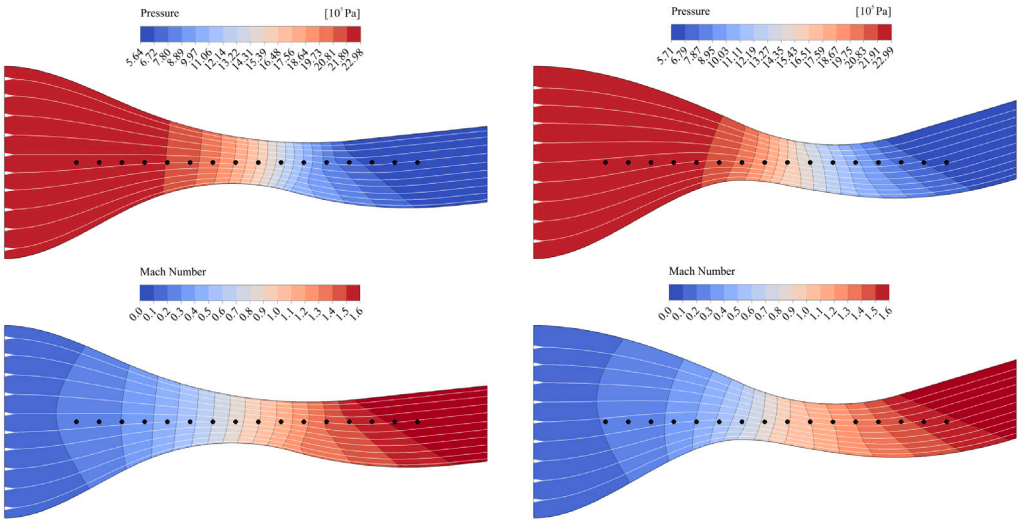

Fig. 2. Inviscid, SW EoS simulation of the flow in nozzles NMMC01 (a) and NMMC02 (b) under design conditions ($P^t = 23.05 \cdot 10^5$ Pa, $T^t = 537.15$ K, $M_e = 1.6$). Contour bands represent the pressure field (upper row) and the Mach number field (lower row). The black dots on top of the contours are the locations where static pressure is measured. On top of contours, streamlines are reported (white curves).

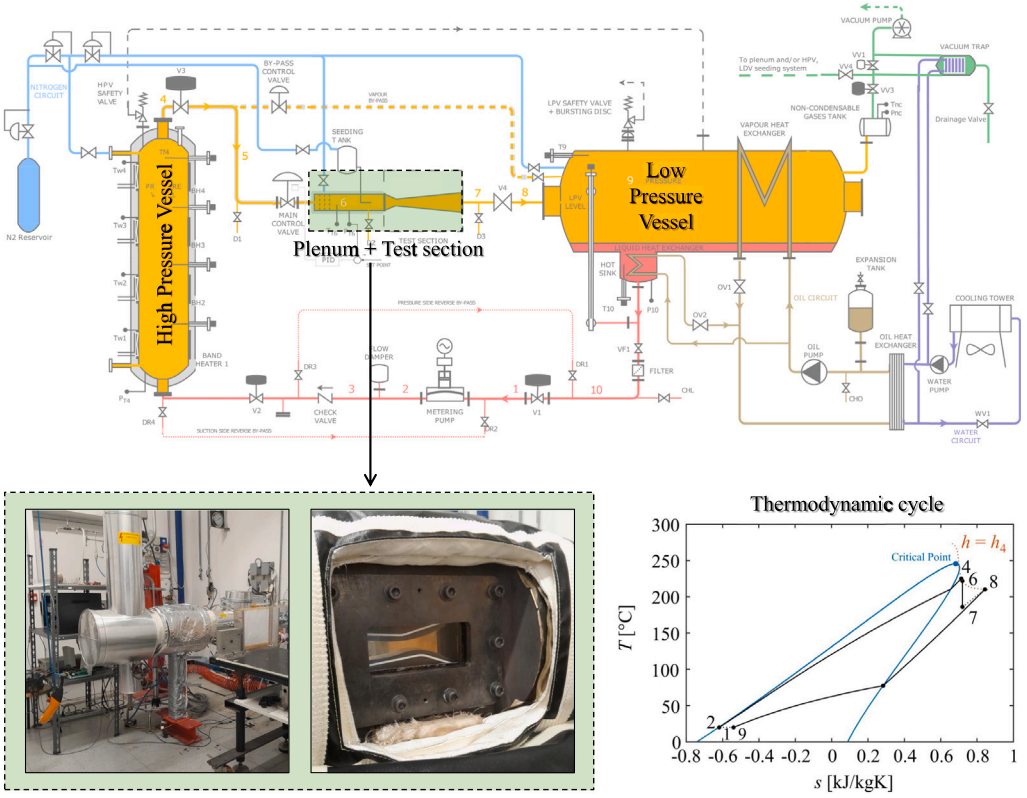

Fig. 3. Layout of the TROVA plant (top). On the bottom row, from left to right, the test section, one of the asymmetric curved nozzles installed in the test section (flow from right to left), and thermodynamic cycle implemented by the TROVA. The numbers on the thermodynamic cycle correspond to the ones reported on the plant scheme. The expansion in the nozzle is 6–7.

the settling chamber using a wall pressure tap, as the kinetic head is negligible due to the low flow velocity (approximately 1 m/s). The total temperature is monitored by two thermocouples located at the symmetry axis of the plenum. Pressure sensors are calibrated for both pressure and temperature (0.35–4 MPa, 298–573 K) and have an expanded uncertainty of 0.07% of full scale. Thermocouples are calibrated for 473–533 K and have an uncertainty of about 1 K. Under the operating conditions of these tests, the expected uncertainty for pressure measurements is a maximum of approximately $0.04 \cdot 10^5$ Pa for total pressure and about $0.015 \cdot 10^5$ Pa for static pressures. More information regarding the pressure and temperature measurement system of the TROVA and the definition of the corresponding measurement uncertainties can be found in Ref. [17].

Fig. 4 illustrates the geometries of the tested nozzles. The blue line marks the horizontal symmetry axis of the test section, where 16 wall pressure taps are located, referred to as the *pressure taps line*. Due to

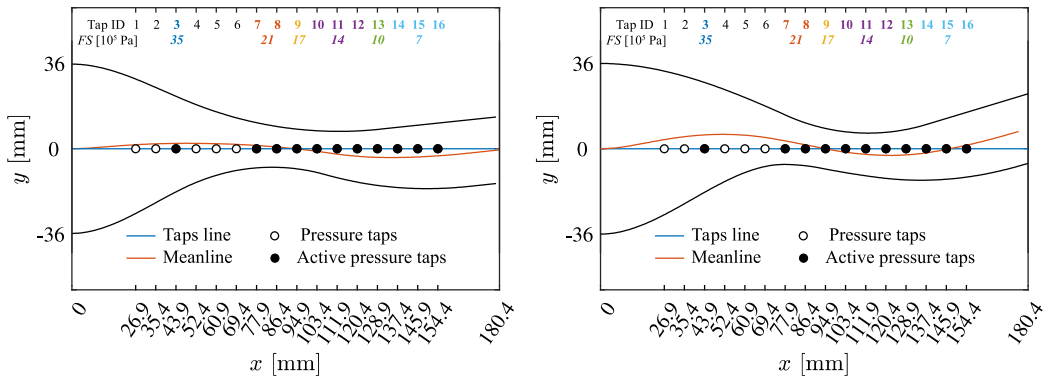

(a) *Nozzle*: NMMC01 (b) *Nozzle*: NMMC02

Fig. 4. Profiles of the nozzles tested in the test section. The figures highlight the pressure taps along the horizontal axis of the test section, the geometric mean lines of the nozzles, and the full scale of the pressure transducers.

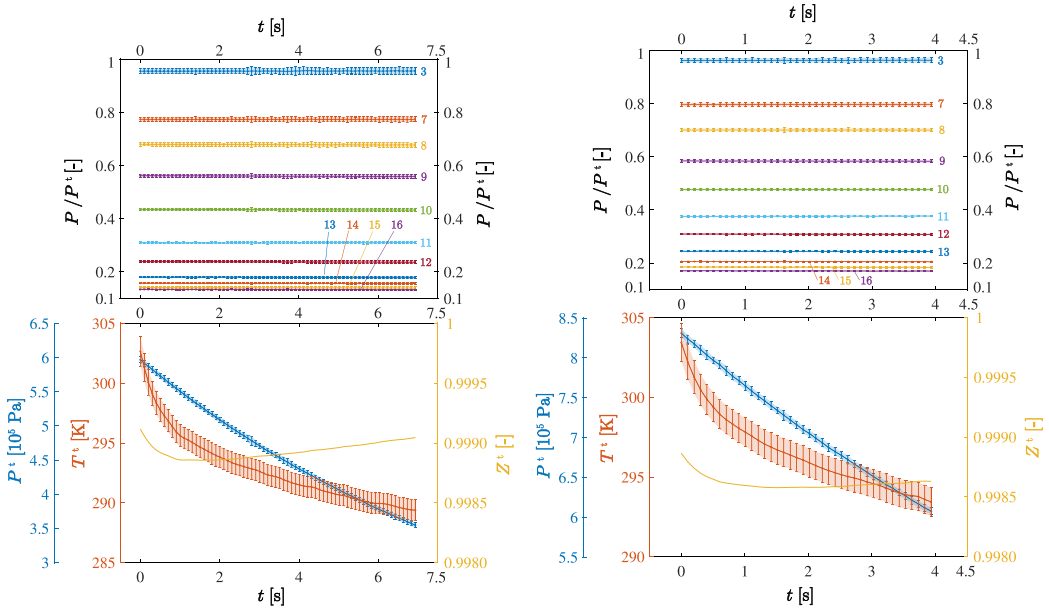

(a) *Nozzle*: NMMC01
Test: NMMC01-N2-008

(b) *Nozzle*: NMMC02
Test: NMMC02-N2-004

Fig. 5. N_2 tests – (Upper row) Time histories of the measured pressure ratios P/P^t, where the numbers on the graphs identify the pressure taps (cf. Fig. 4). (Lower row) Time histories of P^t and T^t, measured in the plenum, and of $Z^t(P^t, T^t)$, computed using the SW EoS.

the nozzle mean line curvature, this line is not a line of symmetry, and the velocity angle is expected to be non-zero along it. The orange line indicates the geometrical mean line of the nozzles, highlighting their curvature from inlet to outlet. During experiments, static pressure is measured at locations indicated by filled black circles, labeled as *active pressure taps* in Fig. 4. The identification numbers of the pressure taps and the full scale (FS) of the pressure transducers are provided in the upper part of the graphs and will be used to correlate the pressure signals in this paper. The x-axis ticks in this and all subsequent figures reporting pressure measurements along the pressure taps line are set to reflect the exact axial positions of the pressure taps. Schlieren visualizations, using the double-passage parallel-light setup from Ref. [30], complement pressure and temperature measurements. In this study, a CMOS camera captures schlieren images at a resolution of 1936×1216 pixels, 20 fps, and 0.9 ms exposure. The schlieren knife is oriented to display density gradients in the axial direction. The schlieren technique is suitable for characterizing nonideal supersonic flows due to its non-invasive nature and simplicity, unlike Laser Doppler Velocimetry (LDV) and Particle Image Velocimetry (PIV), which require particle seeding in high-pressure, high-temperature flows. The technique presented in Ref. [24] is applied to schlieren images to measure the Mach number in the diverging nozzle section (see Fig. 9). The process for measuring flow Mach number from schlieren images is outlined in Section 4.2 and supported by experimental results.

4. Results

The nozzles NMMC01 and NMMC02 are initially tested by operating the wind tunnel with nitrogen. These preparatory tests aim to evaluate the pressure and temperature measurement chain, assess test repeatability, and verify that the measured flow aligns with the ideal gas model. The nozzles are subsequently tested with siloxane MM, complementing pressure and temperature measurements with optical techniques for flow visualization. The objectives of the tests with MM are to evaluate the performance of the nozzles with the design working fluid and to characterize the flow under nonideal conditions. Section 4.1 discusses the nitrogen tests, Section 4.2 covers the MM tests, while Table 1 lists the properties of both fluids.

Table 1
Properties of the working fluids used in the experiments.

Fluid name	Formula	M_w [kg/kmol]	T_c [K]	P_c [10^5 Pa]	ρ_c [kg/m^3]	γ^0 [–]
Nitrogen	N_2	28.01348	126.19	33.95800	313.30	1.3999
MM	$C_6H_{18}OSi_2$	162.37752	518.75	19.39000	258.15	1.0255

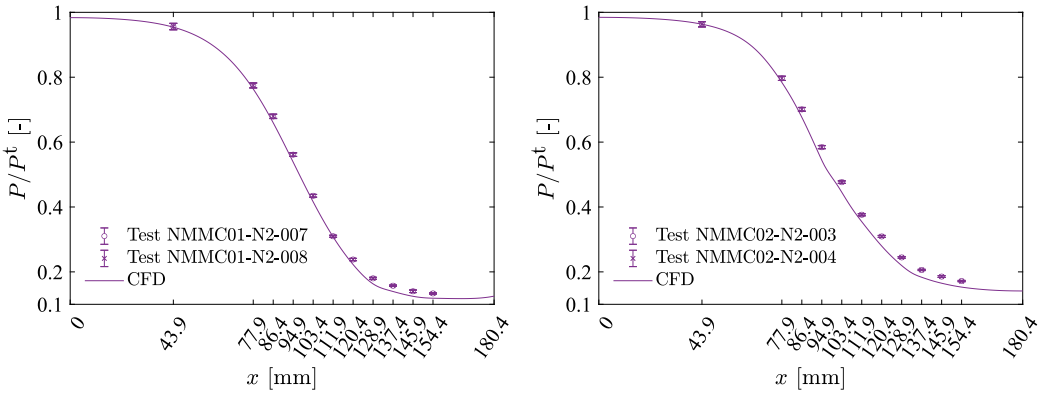

(a) *Nozzle*: NMMC01 (b) *Nozzle*: NMMC02

Fig. 6. N_2 tests — Repeatability assessment and comparison with inviscid CFD (perfect gas). The graphs display the pressure ratios P/P^t measured at one fixed time instant per test, for two repetitions of the experiment.

4.1. Experiments with nitrogen

Several preparatory nitrogen tests were conducted at room temperature by establishing a pressure difference between HPV and LPV to achieve adapted flow conditions within the nozzles for a few seconds of data acquisition. For two such tests, one for each nozzle, Fig. 5 shows the time histories of the measured temperatures and pressures. All pressure measurements reported in this work, including those shown in pressure ratios, refer to absolute pressure values. The plots in the lower row of Fig. 5 present the time histories of the total pressure P^t and total temperature T^t measured in the plenum, along with their expanded uncertainties. The third axis on the right shows the compressibility factor under total conditions Z^t, calculated as a function of (P^t, T^t) using the SW EoS. Both Figs. 5(a) and 5(b) illustrate a decrease in P^t and T^t over testing time, indicating the emptying of the HPV (see Section 3) during the test. In contrast, Z^t remains approximately constant throughout the test at around ∼1, confirming that the perfect-gas law effectively models the fluid's thermodynamics. Since the absolute values of (P^t, T^t) do not affect the flow pattern in the nozzle within the observed range of (P^t, T^t) in these experiments, where the perfect-gas model applies, both the pressurization/depressurization of the reservoirs and the data acquisition are adjusted manually, without precisely controlling the setpoints in terms of pressure and temperature. Therefore, the differences in the ranges of P^t and the durations of the tests seen in Figs. 5(a) and 5(b) can be attributed to this testing procedure. The graphs in the upper row of Fig. 5 show static-to-total pressure ratios along the horizontal axis. Static pressures are recorded at the pressure taps in Fig. 4, while total pressure is measured in the plenum. The numbered labels on the graphs correspond to the pressure taps. Uncertainty bars in the P/P^t plots of Fig. 5 are calculated from measurement uncertainties of P and P^t. According to the perfect-gas model, the pressure ratios P/P^t remain consistent during the test duration. Since the TROVA is a blow-down facility, the measured P/P^t remains constant across varying (P^t, T^t). The repeatability of the measurements is assessed by extracting the pressure ratio profiles $P/P^t(x)$ at a fixed time point for two repetitions of the experiment. Repeatability results are shown in Fig. 6, where experimental data are compared with inviscid CFD simulations. For both nozzles, the uncertainty bars of repeated measurements of P/P^t overlap nearly perfectly at all positions along the axis of the test section, demonstrating the repeatability of the measurements. The agreement with inviscid CFD simulations run using the perfect-gas model is satisfactory and comparable to previous experimental campaigns executed in the same facility, cf. Ref. [23]. Additionally, the measured P/P^t profiles indicate that the flow within both nozzles is free of shock waves, even for nozzle NMMC02 (Type II, cf. Section 3), which would intuitively be more susceptible to shock formation under off-design conditions due to the concordant curvature of its upper and lower contours.

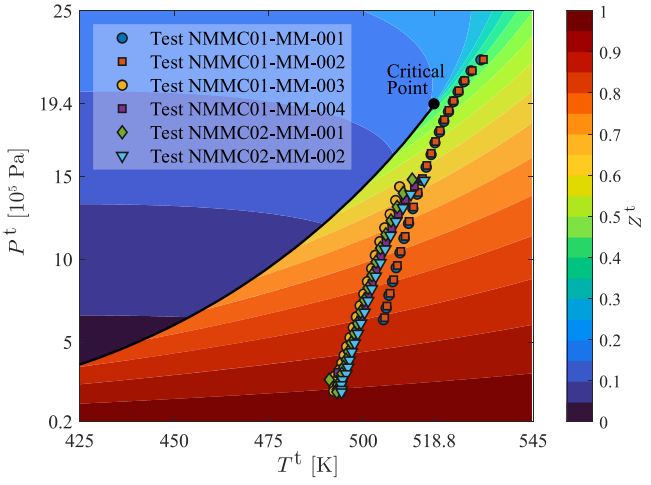

Fig. 7. MM tests – P-T diagram of MM. The axes represent total conditions (P^t, T^t) and the symbols identify the measured (P^t, T^t) over testing time. The colored contour bands show the distribution of $Z^t(P^t, T^t)$ computed using the SW EoS.

4.2. Experiments with siloxane MM

Tests with MM were conducted under the operating conditions summarized in the P-T diagram in Fig. 7. The axes represent the total conditions (P^t, T^t), and the symbols in the graph indicate the (P^t, T^t) measured throughout the test duration. The colored contour bands illustrate the distribution of $Z^t(P^t, T^t)$, computed using the SW EoS. Z^t indicates the deviation of the volumetric behavior of a

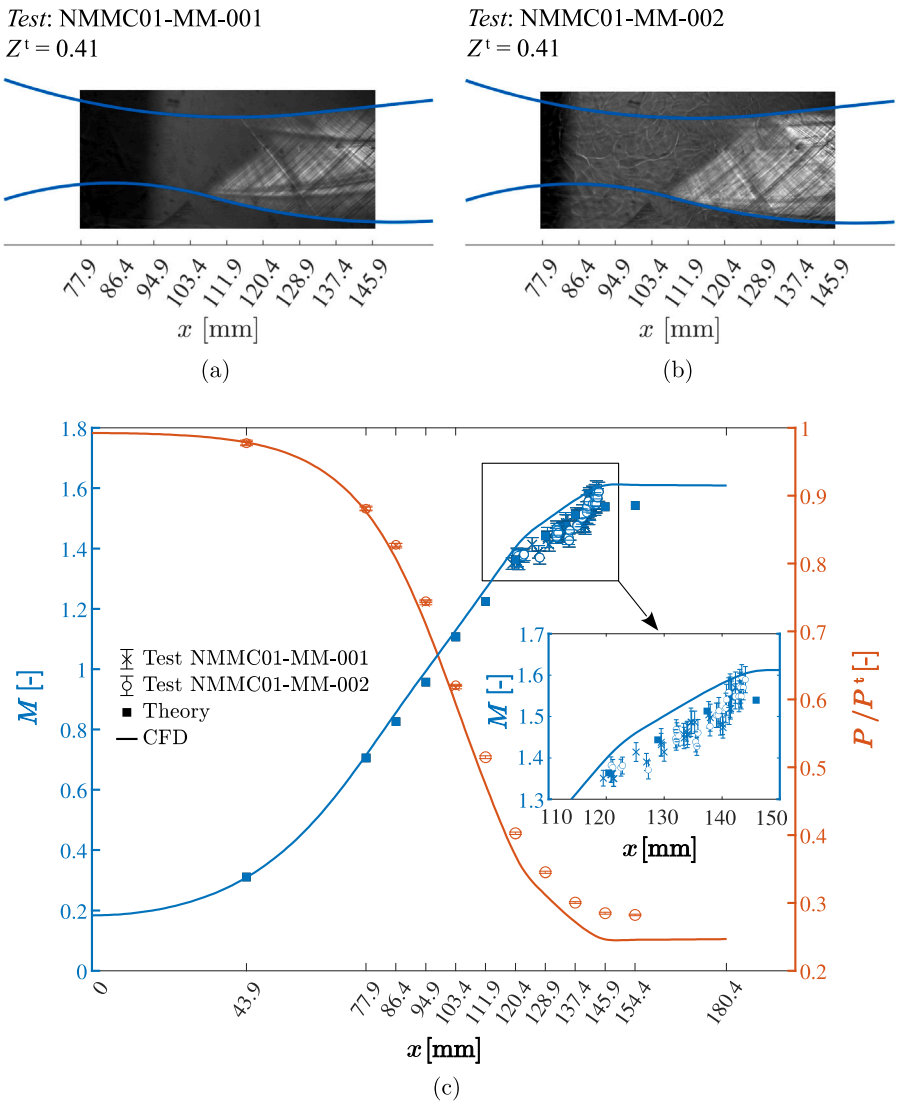

Fig. 8. MM tests – (a, b) Schlieren visualizations in operating conditions characterized by $Z^t = 0.41$ (see Table 2). (c) Repeatability assessment: the measured P/P^t and M are reported for two repetitions of the experiment and compared to inviscid CFD. The theoretical values of M computed from the P profile measured in Test NMMC01-MM-002 are also reported.

flow from that of an ideal gas, thereby quantifying the level of flow nonideality. For nozzle NMMC01, tests are conducted both near the nozzle's design point in the supercritical region and in off-design, fully subcritical states. For nozzle NMMC02, tests are carried out in subcritical conditions only. Despite extensive experience with wind tunnel operations, several challenges hinder the repeatability of measurements in tests starting from supercritical states and near saturation conditions. These challenges include the lengthy preparation time required for each test (up to several days), stress on wind tunnel components and instrumentation (such as gaskets and flush-mounted pressure transducers) due to high operating pressures and temperatures, and difficulties in controlling the overall conditions in the plenum (see Ref. [31]). Therefore, most tests presented in this article are carried out under subcritical conditions, making it easier to achieve satisfactory measurement repeatability and resulting in fewer uncertainties compared to supercritical conditions. The conditions in Table 2 are selected for further analysis in the remainder of the article. The repeatability of measurements is evaluated by comparing results from different test repetitions at the same Z^t value, adhering to the procedure outlined by [17,32]. Z^t constitutes indeed a suitable similarity parameter for complex fluids under moderately high nonideal conditions.

Experiments with nozzle NMMC01 at $Z^t = 0.41$, close to the nozzle's design point, are examined first, as shown in Fig. 8. The total conditions are supercritical in both pressure and temperature. Schlieren images for $Z^t = 0.41$ are displayed for two repeated tests in Figs. 8(a) and 8(b). All schlieren visualizations presented in this work, including these, focus on the optically accessible portion of the nozzle, with flow direction consistently from left to right. In these grayscale images, darker gray levels represent positive density gradients (compressions), while lighter gray levels indicate negative density gradients (expansions). Mach waves, arising from machining imperfections of the contoured profiles, are visible in both images. The nozzle profiles are intentionally left unpolished to highlight the Mach waves in the schlieren visualizations. Specifically, the internal surface finish of the wetted nozzle walls is specified as Ra = 1.6 μm, corresponding to a standard machined finish.

In both Figs. 8(a) and 8(b), a large portion of the image appears fully dark, limiting the measurement area. This well-documented effect, extensively studied by [30], arises from the high flow compressibility that leads to measurement range issues. Furthermore, Fig. 8(a), and to a lesser extent Fig. 8(b), exhibit a few spurious traces. These traces result from minor dirt transported from upstream pipes and valves at the beginning of the test, which becomes trapped in the boundary

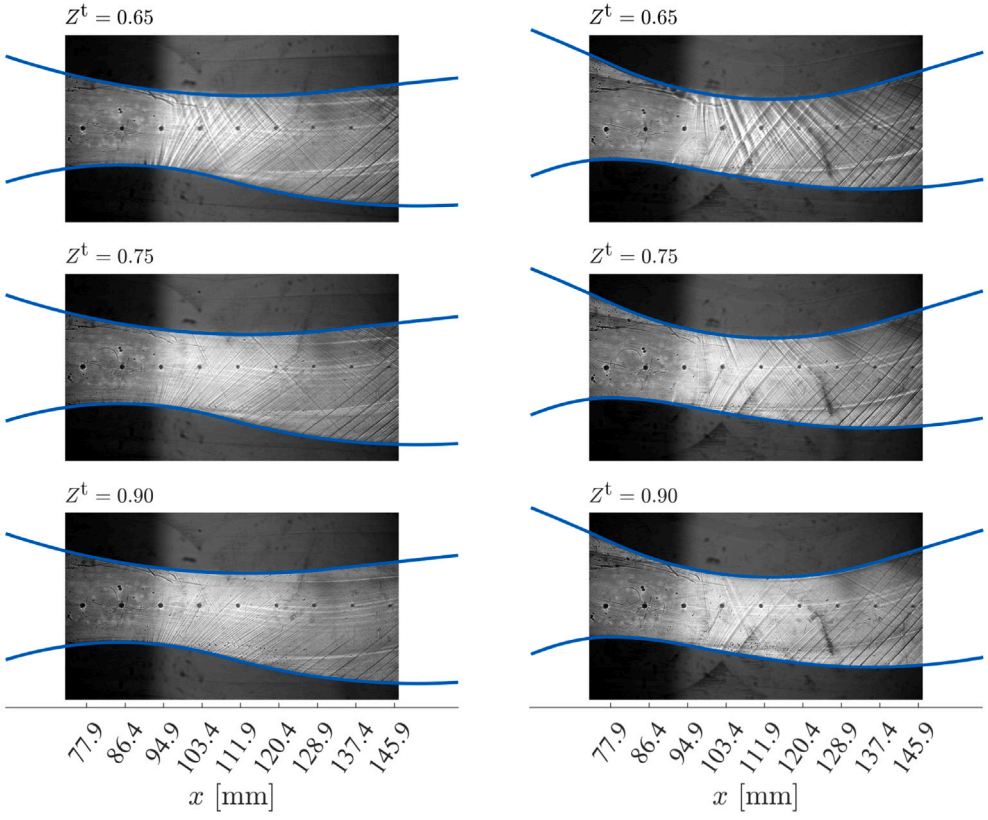

(a) *Nozzle*: NMMC01
Test: NMMC01-MM-004

(b) *Nozzle*: NMMC02
Test: NMMC02-MM-001

Fig. 9. MM tests — Schlieren visualizations in operating conditions characterized by $Z^t = 0.65$, $Z^t = 0.75$, and $Z^t = 0.90$, see Table 2.

Table 2
MM tests — List of the operating conditions studied in this work. The measured P^t and T^t are reported with their expanded uncertainties U_{P^t} and U_{T^t}, respectively. The total compressibility factor Z^t is computed using the SW EoS from the nominal (P^t, T^t).

(a) *Nozzle*: NMMC01

Test	Z^t [–]	$P^t \pm U_{P^t}$ [10^5 Pa]	$T^t \pm U_{T^t}$ [K]
NMMC01-MM-001	0.41	20.896 ± 0.049	527.19 ± 1.18
NMMC01-MM-002	0.41	20.970 ± 0.078	527.49 ± 1.18
NMMC01-MM-003	0.65	13.372 ± 0.035	508.37 ± 1.15
	0.75	10.015 ± 0.035	503.04 ± 1.14
	0.90	4.253 ± 0.033	495.01 ± 1.13
NMMC01-MM-004	0.65	13.761 ± 0.038	511.78 ± 1.15
	0.75	10.144 ± 0.035	504.68 ± 1.14
	0.90	4.309 ± 0.033	496.68 ± 1.13

(b) *Nozzle*: NMMC02

Test	Z^t [–]	$P^t \pm U_{P^t}$ [10^5 Pa]	$T^t \pm U_{T^t}$ [K]
NMMC02-MM-001	0.65	13.507 ± 0.036	509.60 ± 1.15
	0.75	10.066 ± 0.034	503.75 ± 1.14
	0.90	4.283 ± 0.032	495.86 ± 1.13
NMMC02-MM-002	0.65	13.844 ± 0.036	512.48 ± 1.15
	0.75	10.185 ± 0.033	505.19 ± 1.14
	0.90	4.320 ± 0.032	496.96 ± 1.13

layer throughout the test and is notably highlighted by the schlieren visualization. These small impurities do not impact the measurements and are not physically significant.

A line detection algorithm is employed to extract the slopes of Mach waves from schlieren images, enabling the determination of local flow angles and Mach numbers at their intersections. These waves appear in the supersonic, diverging section of the nozzle and exhibit slopes of the form $\vartheta \pm \mu$, where ϑ is the local flow direction and $\mu = \arcsin(1/M)$ is the Mach angle, with M being the local Mach number. The bisector of the intersecting Mach lines indicates the local flow direction. Only intersections within 0.4 mm of the pressure tap line are considered, ensuring both a sufficient number of data points and consistency with the reference pressure measurements. The pressure taps have a diameter of 0.3 mm. This technique, independent of the thermodynamic model adopted for the fluid, is applicable to both dilute gas and nonideal compressible flows. It is described in detail in Ref. [24]. In this work, it is used to extract local Mach numbers along the horizontal axis of the test section, where the pressure taps are located. It is important to note that this axis is not a symmetry line of the nozzle due to its asymmetric, curved geometry, and the local flow direction ϑ along it is not known a priori. The slopes of the intersecting Mach waves are determined by the detection algorithm and are subject to uncertainty, which depends on the schlieren image resolution and the apparent line thickness. While a full description is provided in Ref. [24], the key result relevant to the uncertainty analysis in this work is the expression for the expanded uncertainty of the Mach number: $U_M = M\sqrt{M^2-1}\,U_\mu$, where U_μ is the expanded uncertainty (at 95% confidence level) of the Mach angle μ. As expected, U_M increases with Mach number due to the nonlinear dependence of M on μ through the inverse sine function. Specifically, the uncertainty grows proportionally to M^2, leading to larger errors at higher Mach numbers.

The pressure ratios P/P^t and the local Mach number M measured at $Z^t = 0.41$ are reported for both repeated tests NMMC01-MM-001 and NMMC01-MM-002 in Fig. 8(c). These values are compared to inviscid CFD results using the SW EoS (CFD), as well as to values (Theory) computed under the assumption of steady, isentropic, one-dimensional flow (constant $h^t(P^t, T^t)$ and $s(P^t, T^t)$), based on static pressures measured along the axis. The thermodynamic properties in

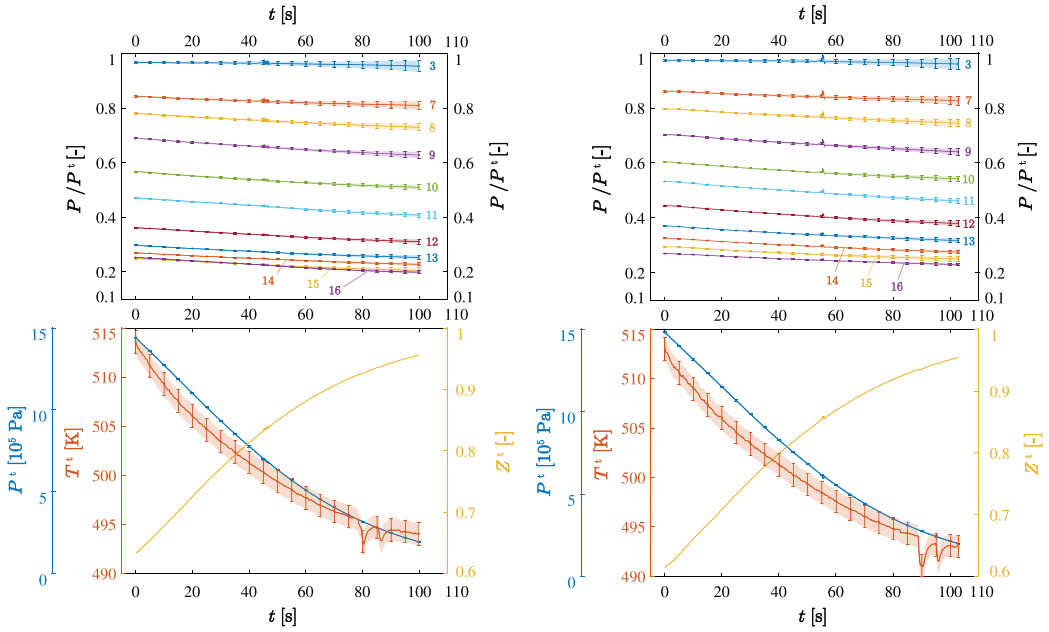

(a) *Nozzle*: NMMC01
Test: NMMC01-MM-004

(b) *Nozzle*: NMMC02
Test: NMMC02-MM-001

Fig. 10. MM tests – (Upper row) Time histories of the measured pressure ratios P/P^t (top), where the numbers on the graphs identify the pressure taps (cf. Fig. 4). (Lower row) Time histories of P^t and T^t, measured in the plenum, and of $Z^t(P^t, T^t)$, computed using the SW EoS.

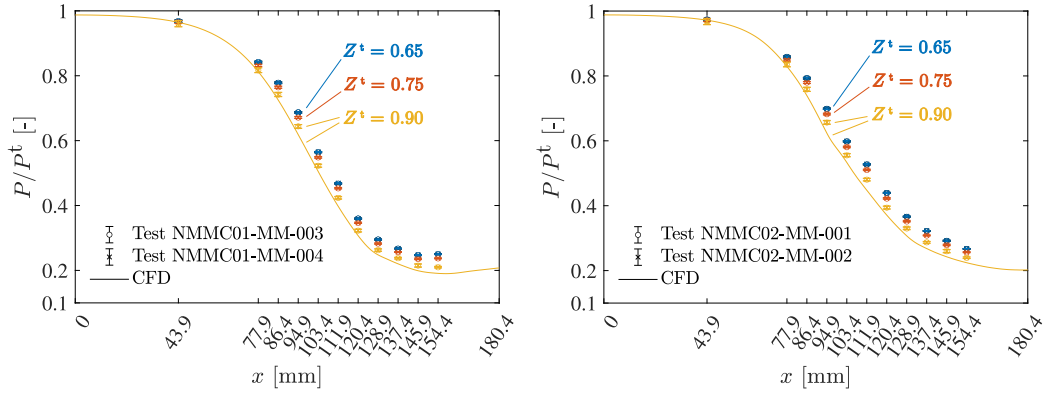

(a) *Nozzle*: NMMC01

(b) *Nozzle*: NMMC02

Fig. 11. MM tests — Repeatability assessment and comparison with inviscid CFD ($Z^t = 0.90$). The graphs display the ratios P/P^t measured at selected Z^t, for two repetitions of the experiment. Test conditions are reported in Table 2.

the theoretical model are calculated using the SW EoS. Mach number measurements are based on the schlieren frames in Figs. 8(a) and 8(b), which demonstrate acceptable quality for detecting Mach lines. The zoomed area in Fig. 8(c) reveals noticeable variability in repeated M measurements, particularly near the exit section, where higher Mach numbers are reached and measurement uncertainties are most significant. Nonetheless, the uncertainty bars for M at matching locations show satisfactory overlap and a consistent overall trend. From Fig. 8(c), the uncertainty bars for P/P^t nearly perfectly overlap until pressure tap 10 ($x = 103.4$ mm from the inlet). Beyond this point, only P/P^t measurements from test NMMC01-MM-002 are reported, as multiple outliers in test NMMC01-MM-001 were excluded due to measurement issues. Although the repeatability of P/P^t measurements for $x > 103.4$ mm is not thoroughly assessed by comparing both tests, the validity of P/P^t measurements from test NMMC01-MM-002 is indirectly supported through Mach number comparisons. The Mach number computed from one-dimensional theory based on the pressures measured in test NMMC01-MM-002 agrees satisfactorily with the measured Mach numbers in both tests, thus validating the P/P^t values from test NMMC01-MM-002. The agreement with inviscid CFD simulations at this level of nonideality ($Z^t = 0.41$) is comparable to previous experimental campaigns carried out in the same facility (cf. Ref. [31]).

In tests conducted under fully subcritical conditions, both nozzles exhibit a shock-free flow pattern in the divergent section, as illustrated in Fig. 9, which presents the schlieren images captured for $Z^t = 0.65, 0.75, 0.90$. The Mach lines are apparent in all frames, though they become less distinct as Z^t increases due to decreased compressibility. For this reason, the entire optically accessible area is visible, unlike the frames shown in Figs. 8(a) and 8(b). Although the Mach wave trains appear prominently in the schlieren images, they are, by definition, shocks of infinitesimal strength and do not significantly alter the flow field. This observation is consistent with previous numerical and experimental studies (e.g., Refs. [17,23]), which confirm that the flow retains the isentropic expansion characteristics predicted by inviscid modeling, with negligible influence from viscous dissipation or surface roughness

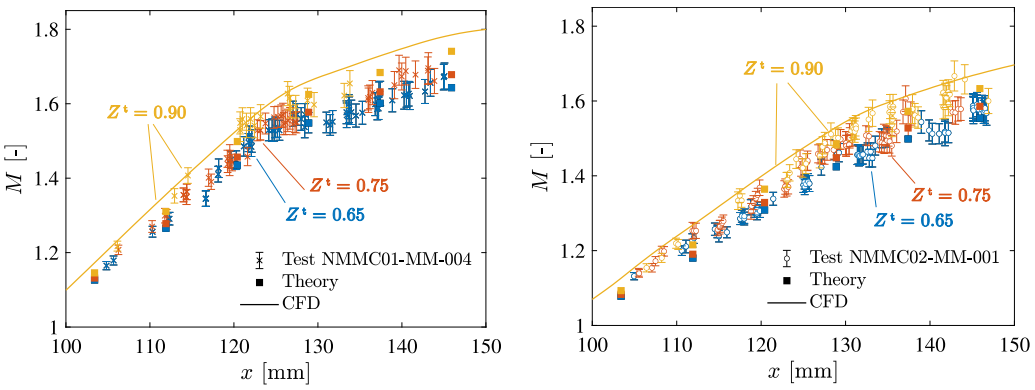

(a) *Nozzle*: NMMC01
Test: NMMC01-MM-004

(b) *Nozzle*: NMMC02
Test: NMMC02-MM-001

Fig. 12. MM tests — Mach number measured along the taps line at selected Z^t, compared to inviscid CFD ($Z^t = 0.90$) and to the theoretical values of M computed from the P profiles measured at all Z^t. Test conditions are reported in Table 2.

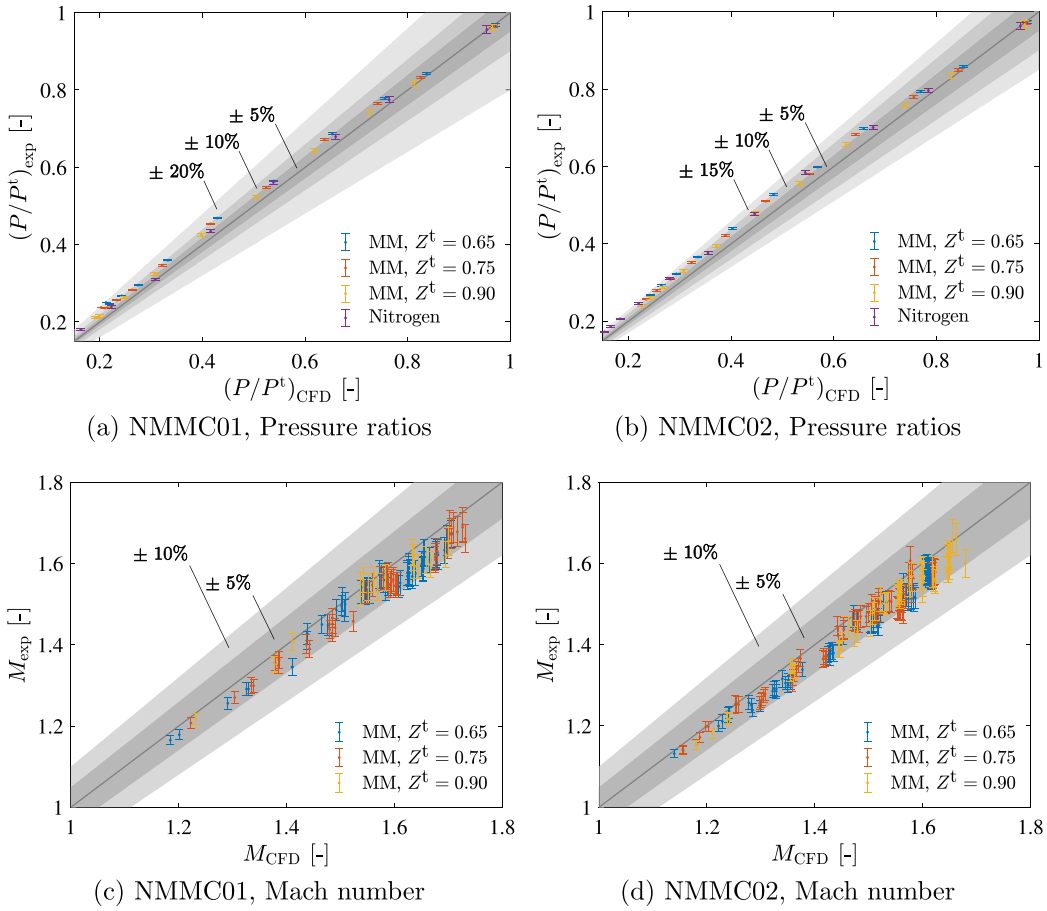

(a) NMMC01, Pressure ratios

(b) NMMC02, Pressure ratios

(c) NMMC01, Mach number

(d) NMMC02, Mach number

Fig. 13. Parity plots for P/P^t (a, b) and M (c, d) in nozzle NMMC01 (a, c) and NMMC02 (b, d). Measurements are compared to inviscid CFD results. Simulations with MM are run using the SW EoS, while simulations with N_2 are run using the ideal-gas model.

effects. Notably, this conclusion is supported not only by simulations but also directly by the experimental measurements presented in this work. The absence of shocks in the divergent section throughout the test duration is confirmed for both nozzles by the results in Fig. 10. Similarly to the Nitrogen tests (cf. Fig. 5), Fig. 10 shows the time histories of P/P^t, P^t, T^t, and Z^t for two representative MM tests with nozzles NMMC01 (Fig. 10(a)) and NMMC02 (Fig. 10(b)). The compressibility factor $Z^t(P^t, T^t)$ increases during the tests due to the HPV emptying process, but remains below 1. The decreasing trend of P/P^t indicates nonideal effects in the expansion of MM in the nozzles. In contrast to the constant P/P^t observed in Nitrogen tests, the pressure ratios P/P^t vary with (P^t, T^t) at all points along the pressure taps line.

The repeatability of measurements is evaluated by the pressure ratios P/P^t at the same Z^t for two repetitions of the experiment. Fig. 11 shows that uncertainty bars from repeated measurements of P/P^t overlap nearly perfectly at all pressure tap locations and for all Z^t, illustrating measurement repeatability. Experimental data are

compared with inviscid CFD simulations at $Z^t = 0.90$. The flow layout under the conditions in Fig. 11 is shown in the schlieren frames of Fig. 9. Results indicate that lower Z^t, or greater nonideality leads to higher pressure ratios P/P^t at all x locations, aligning with NICFD theory and previous observations of supersonic expansions in planar symmetric nozzles [16].

Mach number measurements are taken along the pressure taps line in the divergent sections of both nozzles for these conditions. Fig. 12 compares the experimental data with the theoretical values of the Mach number computed from the measured pressure profiles at all Z^t and with inviscid CFD at $Z^t = 0.90$. Parity plots are reported in Fig. 13. The measured values of M increase with higher Z^t, consistent with one-dimensional theory. Despite some overlap in the measurement uncertainties, this trend is observable in the experimental results.

5. Conclusions

An experimental campaign investigated the supersonic expansion of linear siloxane MM (hexamethyldisiloxane, $C_6H_{18}OSi_2$) in asymmetric curved planar nozzles. The tests were performed in a supersonic blow-down wind tunnel, the Test Rig for Organic Vapours (TROVA) at Politecnico di Milano. Two different asymmetric curved planar nozzles were tested using nitrogen and siloxane MM in subcritical and supercritical conditions. The nozzles feature gently-curved mean lines from the inlet to the outlet sections, discharging flow at geometric deviations of 6° and 17° from the horizontal.

Shock-free expansions were observed under all tested conditions, ranging from highly nonideal ($Z^t = 0.41$) to ideal-like ($Z^t = 0.95$), thus confirming the initial design. Total pressure, temperature, static pressures from the inlet to the outlet, and schlieren images were recorded for each condition to measure the Mach number.

Experimental results compare fairly well with numerical simulations of the flow field, in terms of the Mach number and the pressure ratio measured at selected locations. Nonideal effects have been observed. In particular, the measured values of the Mach number increase and the static-to-total pressure ratios decrease with higher Z^t, consistent with one-dimensional theory.

The experimental data presented in this study serve as a reference for benchmark asymmetric nozzle geometries operating in the nonideal regime, which until now had only been validated through numerical simulations. These results can be directly used to validate CFD models or design tools employed in the development of ORC turbine stators. By offering both detailed geometrical definitions and experimental data points, this work supports the broader research community in improving the accuracy and reliability of simulation-based design approaches. The full dataset is made available in the Supplemental Material to facilitate reproducibility and further application.

CRediT authorship contribution statement

Marta Zocca: Writing – original draft, Methodology, Investigation, Data curation, Conceptualization. **Paolo Gajoni:** Writing – review & editing, Methodology, Data curation. **Alberto Guardone:** Writing – review & editing, Methodology, Conceptualization.

Declaration of Generative AI and AI-assisted technologies in the writing process

During the preparation of this work the authors used Microsoft Copilot in order to check language and readability. After using this tool/service, the authors reviewed and edited the content as needed and takes full responsibility for the content of the publication.

Declaration of competing interest

The authors declare that they have no known competing financial interests or personal relationships that could have appeared to influence the work reported in this paper.

Acknowledgments

This research was funded by the Research Council of Finland under Grant number 342135, project *Non-ideal compressible flows in turbomachinery*. The authors thank Dr. Camilla Cecilia Conti and Ms. Francesca Mondonico for their support during all experimental runs.

Appendix A. Supplementary data

Supplementary material related to this article can be found online at https://doi.org/10.1016/j.applthermaleng.2025.127473.

Data availability

The authors are unable or have chosen not to specify which data has been used.

References

[1] A. Guardone, P. Colonna, M. Pini, A. Spinelli, Nonideal compressible fluid dynamics of dense vapors and supercritical fluids, Annu. Rev. Fluid Mech. 56 (2024) 241–269, http://dx.doi.org/10.1146/annurev-fluid-120720-033342.

[2] J. Bellan (Ed.), High-Pressure Flows for Propulsion Applications, in: Progress in Astronautics and Aeronautics, vol. 260, American Institute of Aeronautics and Astronautics, 2020, http://dx.doi.org/10.2514/4.105814.

[3] J. Maincent, R.O. Williams, Precipitation technologies for nanoparticle production, in: R. Williams, A. Watts, D. Miller (Eds.), Formulating Poorly Water Soluble Drugs, in: AAPS Advances in the Pharmaceutical Sciences, vol. 3, Springer, 2016, pp. 609–689, http://dx.doi.org/10.1007/978-1-4614-1144-4_12.

[4] M.T. White, G. Bianchi, L. Chai, S.A. Tassou, A.I. Sayma, Review of supercritical CO_2 technologies and systems for power generation, Appl. Therm. Eng. 185 (2021) 116447, http://dx.doi.org/10.1016/j.applthermaleng.2020.116447, 28 pages.

[5] E. Macchi, M. Astolfi (Eds.), Organic Rankine Cycle (ORC) Power Systems: Technologies and Applications, in: Woodhead Publishing Series in Energy, Woodhead Publishing, 2017, http://dx.doi.org/10.1016/C2014-0-04239-6.

[6] A. Romei, D. Vimercati, G. Persico, A. Guardone, Non-ideal compressible flows in supersonic turbine cascades, J. Fluid Mech. 882 (2020) A12, http://dx.doi.org/10.1017/jfm.2019.796, 26 pages.

[7] D. Baumgärtner, J.J. Otter, A.P.S. Wheeler, The effect of isentropic exponent on transonic turbine performance, J. Turbomach. 142 (8) (2020) 081007, http://dx.doi.org/10.1115/1.4046528, 10 pages.

[8] M. Manfredi, G. Persico, A. Spinelli, P. Gaetani, V. Dossena, Design and commissioning of experiments for supersonic ORC nozzles in linear cascade configuration, Appl. Therm. Eng. 224 (2023) 119996, http://dx.doi.org/10.1016/j.applthermaleng.2023.119996, 11 pages.

[9] A. Spinelli, A. Guardone, C.D. Servi, P. Colonna, F. Reinker, S. aus der Wiesche, M. Robertson, R.F. Martinez-Botas, Experimental facilities for non-ideal compressible vapour flows, in: M. Marek (Ed.), ERCOFTAC Bulletin Nr. 124, ERCOFTAC, 2020, pp. 59–66, URL https://www.ercoftac.org/downloads/watermarks/bulletin-docs/bulletin_124.pdf.

[10] F. Reinker, R. Wagner, L. Hake, S. aus der Wiesche, High subsonic flow of an organic vapor past a circular cylinder, Exp. Fluids 62 (3) (2021) 54, http://dx.doi.org/10.1007/s00348-021-03158-y, 16 pages.

[11] F. Beltrame, C. De Servi, A.J. Head, M. Pini, F. Schrijer, P. Colonna, First experiments and commissioning of the ORCHID nozzle test section, in: M. Pini, et al. (Eds.), Proceedings of NICFD 2020, in: ERCOFTAC Series, vol. 28, Springer, 2021, pp. 169–178, http://dx.doi.org/10.1007/978-3-030-69306-0_18.

[12] G. Petruccelli, A. Uusitalo, A. Grönman, T. Turunen-Saaresti, M. Zocca, Closed-loop supercritical carbon dioxide wind tunnel: design and components, in: Conference Proceedings of the European sCO2 Conference4th European sCO2 Conference for Energy Systems: March 23-24 2021, Vol. 2021, 2021, p. 333, http://dx.doi.org/10.17185/DUEPUBLICO/73977.

[13] S.H. Fergason, A. Guardone, B.M. Argrow, Construction and validation of a dense gas shock tube, J. Thermophys. Heat Transfer 17 (3) (2003) 326–333, http://dx.doi.org/10.2514/2.6789.

[14] C. Lettieri, D. Yang, Z. Spakovszky, An investigation of condensation effects in supercritical carbon dioxide compressors, J. Eng. Gas Turbines Power 137 (8) (2015) 082602, http://dx.doi.org/10.1115/1.4029577, 8 pages.

[15] T. Mathijssen, M. Gallo, E. Casati, N.R. Nannan, C. Zamfirescu, A. Guardone, P. Colonna, The flexible asymmetric shock tube (FAST) - a Ludwieg tube facility for wave propagation measurements in high-temperature vapours of organic fluids, Exp. Fluids 56 (10) (2015) 195, http://dx.doi.org/10.1007/s00348-015-2060-1, 12 pages.

[16] A. Spinelli, A. Guardone, F. Cozzi, M. Carmine, R. Cheli, M. Zocca, P. Gaetani, V. Dossena, Experimental observation of non-ideal nozzle flow of siloxane vapor MDM, Energy Procedia 129 (2017) 1125–1132, http://dx.doi.org/10.1016/j.egypro.2017.09.237, 12 pages.

[17] A. Spinelli, G. Cammi, S. Gallarini, M. Zocca, F. Cozzi, P. Gaetani, V. Dossena, A. Guardone, Experimental evidence of non-ideal compressible effects in expanding flow of a high molecular complexity vapor, Exp. Fluids 59 (8) (2018) 126, http://dx.doi.org/10.1007/s00348-018-2578-0, 16 pages.

[18] N. Anand, P. Colonna, M. Pini, Design guidelines for supersonic stators operating with fluids made of complex molecules, Energy 203 (2020) 117698, http://dx.doi.org/10.1016/j.energy.2020.117698.

[19] A. Cappiello, R. Tuccillo, Design and CFD analysis of a radial-inflow turbine for small scale ORC applications, E3S Web Conf. 197 (2020) 11005, http://dx.doi.org/10.1051/e3sconf/202019711005.

[20] H.J. Allen, The Asymmetric Adjustable Supersonic Nozzle for Wind-tunnel Application, RM A8E17, NACA, 1948.

[21] C.A. Syvertson, R.C. Savin, The Design of Variable Mach Number Asymmetric Supersonic Nozzles by Two Procedures Employing Inclined and Curved Sonic Lines, TN 2922, NACA, 1953.

[22] M. Zocca, P. Gajoni, A. Guardone, NIMOC: a design and analysis tool for supersonic nozzles under non-ideal compressible flow conditions, J. Comput. Appl. Math. 429 (2023) 115210, http://dx.doi.org/10.1016/j.cam.2023.115210, 15 pages.

[23] G. Gori, M. Zocca, G. Cammi, A. Spinelli, P.M. Congedo, A. Guardone, Accuracy assessment of the non-ideal computational fluid dynamics model for siloxane MDM from the open-source SU2 suite, Eur. J. Mech. B-Fluid 79 (2020) 109–120, http://dx.doi.org/10.1016/j.euromechflu.2019.08.014.

[24] A. Guardone, M. Zocca, P. Gajoni, F. Mondonico, C.C. Conti, Characteristics-based measurements of supersonic flows from schlieren images, Exp. Fluids 60 (72) (2025) http://dx.doi.org/10.1007/s00348-025-03958-6.

[25] I.H. Bell, J. Wronski, S. Quoilin, V. Lemort, Pure and pseudo-pure fluid thermophysical property evaluation and the open-source thermophysical property library CoolProp, Ind. Eng. Chem. Res. 53 (6) (2014) 2498–2508, http://dx.doi.org/10.1021/ie4033999.

[26] M. Thol, F.H. Dubberke, E. Baumhögger, J. Vrabec, R. Span, Speed of sound measurements and fundamental equations of state for octamethyltrisiloxane and decamethyltetrasiloxane, J. Chem. Eng. Data 62 (9) (2017) 2633–2648, http://dx.doi.org/10.1021/acs.jced.7b00092.

[27] E.W. Lemmon, I.H. Bell, M.L. Huber, M.O. McLinden, NIST Standard Reference Database 23: Reference Fluid Thermodynamic and Transport Properties-REFPROP, Version 10.0, National Institute of Standards and Technology, 2018, http://dx.doi.org/10.18434/T4/1502528, URL https://www.nist.gov/srd/refprop.

[28] M.L. Huber, E.W. Lemmon, I.H. Bell, M.O. McLinden, The NIST REFPROP database for highly accurate properties of industrially important fluids, Ind. Eng. Chem. Res. 61 (42) (2022) 15449–15472, http://dx.doi.org/10.1021/acs.iecr.2c01427.

[29] P.A. Thompson, K.C. Lambrakis, Negative shock waves, J. Fluid Mech. 60 (1973) 187–208, http://dx.doi.org/10.1017/S002211207300011X.

[30] C.C. Conti, A. Spinelli, G. Cammi, M. Zocca, F. Cozzi, A. Guardone, Schlieren visualizations of non-ideal compressible fluid flows, in: 13th International Conference on Heat Transfer, Fluid Mechanics and Thermodynamics, HEFAT, 2017, pp. 513–518, URL https://repository.up.ac.za/bitstream/handle/2263/62466/Conti_Schlieren_2017.pdf?sequence=1.

[31] C.C. Conti, Non-Ideal Compressible Fluid Dynamics of Organic Vapors: From Nozzle Flows to Pressure Probes (Ph.D. thesis), Politecnico di Milano, 2021, URL https://hdl.handle.net/10589/171196.

[32] C.C. Conti, A. Spinelli, A. Guardone, Similarity parameters for non-ideal one-dimensional isentropic expansions, in: M. Pini, et al. (Eds.), Proceedings of NICFD 2020, in: ERCOFTAC Series, vol. 28, Springer, 2021, pp. 26–35, http://dx.doi.org/10.1007/978-3-030-69306-0_4.